

An Active Visible-Light Integrated Photonics Platform on 200-mm Si

Wesley D. Sacher^{1,*}, Yiding Lin¹, Hong Chen¹, Saeed S. Azadeh¹, Zheng Yong^{1,2}, Xianshu Luo³, Hongyao Chua³, Jason C. C. Mak², Alperen Govdeli^{1,2}, Ankita Sharma^{1,2}, Jared C. Mikkelsen¹, Xin Mu^{1,2}, Andrei Stalmashonak¹, Guo-Qiang Lo³, Joyce K. S. Poon^{1,2}

¹Max Planck Institute of Microstructure Physics, Weinberg 2, 06120 Halle, Germany

²Department of Electrical and Computer Engineering, University of Toronto, 10 King's College Road, Toronto, Ontario M5S 3G4, Canada

³Advanced Micro Foundry Pte. Ltd., 11 Science Park Road, Singapore Science Park II, 117685, Singapore

*wesley.sacher@mpi-halle.mpg.de

Abstract: We present a foundry-fabricated monolithically integrated photonics platform for the visible spectrum ($\lambda=445\text{--}640\text{nm}$) with two layers of silicon nitride waveguides, silicon photodiodes, efficient undercut thermo-optic phase shifters, *in situ* trimming, and electro-thermal MEMS devices. © 2023 The Author(s)

Recent demonstrations of low-loss, visible-light silicon nitride (SiN) and aluminum oxide waveguides on 200- and 300-mm diameter wafers [1-3] highlight the opportunity for advanced visible-light integrated photonics platforms that rival conventional silicon (Si) photonics platforms in their complexity and manufacturability. Integrated photonics at visible wavelengths can provide unique and scalable solutions for applications including quantum information [4], neurotechnology [5], biosensing [6], and displays [7]. Fully realizing this potential will require photonic integrated circuits (PICs) with active functionality. Recent demonstrations have shown visible-light integrated photonic active devices such as individual phase shifters [8-10], photodetectors [11], and lasers consisting of gain chips co-packaged with SiN PICs [12]. In this work, we present the first visible-light integrated photonics platform with monolithically integrated SiN waveguides, thermo-optic phase shifters, photodetectors, and microelectromechanical systems (MEMS) devices. We reported these devices separately in [13-17], and here, we present the overall photonic platform.

The platform (Fig. 1) was fabricated at Advanced Micro Foundry on 200-mm diameter Si wafers, beginning with forming the photodetectors and waveguide bottom cladding: ion implantation and rapid thermal annealing for the doped Si regions, Si mesa etching, SiO₂ deposition, and chemical mechanical polishing (CMP). Two SiN waveguide layers were defined by plasma enhanced chemical vapor deposition (PECVD) of SiN, ArF deep ultraviolet lithography, and reactive ion etching; CMP was used for layer planarization. Two metal (Al) wiring layers (M1 and M2), vias, and titanium nitride (TiN) heaters were defined next followed by deep trench and undercut etching for suspended structures and edge coupler facets. The platform has 2 SiN waveguide layers, Fig. 1(a); SiN1 has a

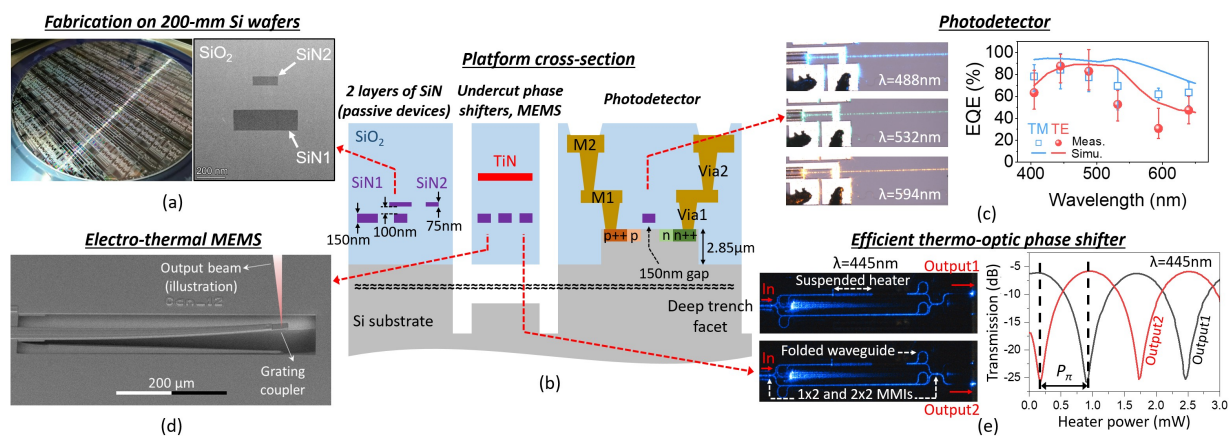


Fig. 1. Visible-light integrated photonics platform. (a) Photograph of a fabricated wafer and cross-section transmission electron micrograph (TEM) of the SiN waveguide layers (SiN1 and SiN2); TEM from [13], scale bar: 200nm. (b) Platform schematic. (c) Photodetector (PD) micrographs with input light. Measured and simulated PD external quantum efficiency (EQE) vs. wavelength (λ); from [14]. The measured data points correspond to the average EQE (over 3 chips), and the bars show the minimum and maximum measured EQE. (d) Scanning electron micrograph of an electro-thermal MEMS cantilever from [17]. (e) Micrographs of the thermo-optic phase shifter integrated into a Mach-Zehnder interferometer (MZI) test structure (suspended heater length $\approx 478\mu\text{m}$) (left); the phase shifter drive power was varied between the micrographs showing switching between the outputs. Measured MZI transmission versus heater power at $\lambda=445\text{nm}$ showing $P_{\pi} = 0.8\text{mW}$ (right); from [15].

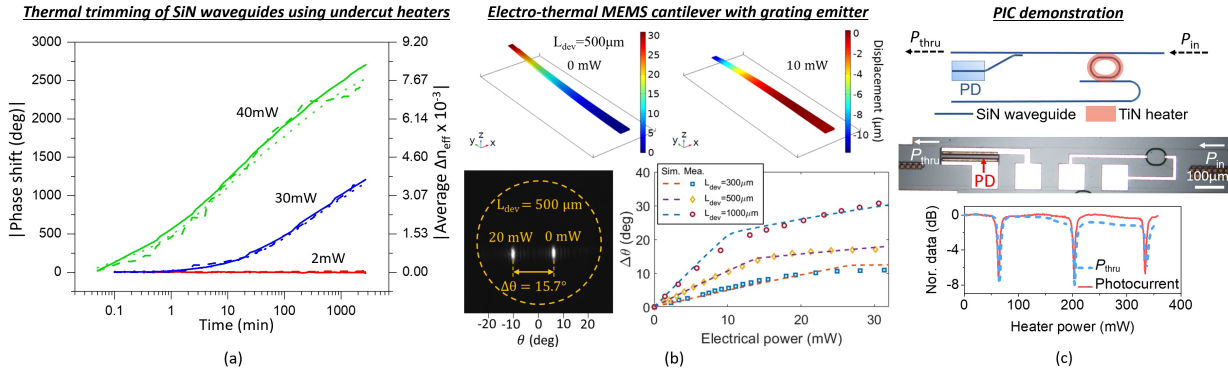


Fig. 2. *In situ* thermal refractive index trimming, MEMS cantilever devices, and PIC demonstration. (a) Waveguide trimming in suspended thermo-optic phase shifters with a single waveguide pass (length=508 μm); solid, dashed, and dotted lines correspond to 3 dies at each heater power (absolute values shown, effective index change, Δn_{eff} , was negative). (b) Electro-thermal MEMS cantilevers with embedded grating coupler emitters. Simulated deflection at 2 heater powers (top), measured far field profiles at 2 heater powers (dashed line = back aperture of the objective lens in the imaging system) (bottom-left), and measured and simulated optical beam deflection ($\Delta\theta$) vs. heater power for 3 cantilever lengths (L_{dev}) (bottom-right); $\lambda=488\text{nm}$, TE polarization, from [17]. (c) Schematic, micrograph, and measurement of a PIC with a thermally-tuned microring and a PD power monitor tap on the thru port. The heater power was swept while the PD photocurrent and thru port optical transmission were measured (input: $\lambda=514\text{nm}$, TE polarization); from [14].

150nm nominal thickness with high optical mode confinement for compact devices, SiN₂ is 75nm thick with relatively low mode confinement, and the 100nm thick interlayer SiO₂ enables efficient interlayer transitions. SiN waveguide losses ($\lambda=430\text{-}648\text{nm}$) were reported in [2,15].

Bi-layer edge couplers: The two waveguide layers enable broadband and low-loss bi-layer edge couplers with visible spectrum single-mode fibers (SMF) [13]. A 240nm wide edge coupler tip in SiN₂ expanded the optical mode to micron-scale to match the SMF. The SiN₂ width was adiabatically increased to a 1 μm width using a 200 μm -long taper for increased optical confinement, and a subsequent 75 μm -long adiabatic interlayer transition coupled light from SiN₂ to a SiN₁ waveguide. The measured fiber coupling efficiency was $> -4\text{dB/facet}$ ($\lambda = 445, 488, 532, 594, 640\text{nm}$) for SMF (Nufern S405-XP).

Photodetectors: The platform has ultra-broadband SiN-on-Si waveguide PIN and PN photodetectors (PDs) [14]. The 150nm nominally thick SiO₂ spacer between SiN₁ and the Si mesas enables efficient light transfer from SiN to Si, where it is absorbed. Figure 1(c) shows the measured (at -2V bias) and simulated external quantum efficiency (EQE) for 50 μm -long PIN PDs with 2 μm -wide intrinsic regions and 200nm-wide SiN₁ waveguides above. The measured EQE was $> 50\%$ for transverse-electric (TE) polarized light at $\lambda = 405, 445, 488, \text{ and } 532\text{nm}$. For TM-polarized light, the measured EQE was $> 60\%$ at several discrete wavelengths from 405 - 640nm. TE operation up to $\lambda = 640\text{nm}$ was also demonstrated but with lower EQE. The opto-electronic (OE) 3-dB bandwidth was about 4.4GHz at -2V bias. The measured dark current was $144 \pm 42\text{pA}$ and $266 \pm 65\text{pA}$ at reverse biases of -5V and -15V, respectively. Avalanche photodetectors were also realized with PN doping. More details are in [14].

Thermo-optic (TO) phase shifters and thermal trimming: The suspended regions in Fig. 1(b), defined by undercut etching through rows of deep trenches, enable efficient TO phase shifters and *in situ* refractive index trimming. The TO phase shifters had TiN heaters and a multi-pass SiN waveguide design within the suspended structure, which provided thermal isolation, similar to infrared Si phase shifters in [18]. The phase shifters were integrated into Mach-Zehnder interferometers (MZIs), and operated at blue, green, and yellow wavelengths (TE polarization) [Fig. 1(e)]; the optical bandwidth was limited by the multimode interference (MMI) couplers of the MZI. The power required for a π phase shift (P_π) was measured to be 0.78, 0.93, 1.09, and 1.20mW at $\lambda = 445, 488, 532, \text{ and } 561\text{nm}$, respectively (averaged over 5 dies, variation $\leq 0.1\text{mW}$ at each λ). The 10-90% rise(fall) time of the MZI switch was about 570(590) μs [15]. Increasing the applied power in the phase shifters to 30-40mW resulted in sufficiently high temperatures (300-400 $^\circ\text{C}$, estimated from simulations) for local thermal refractive index trimming of SiN waveguides. This was tested in suspended TO phase shifters with one waveguide pass in an asymmetric MZI, Fig. 2(a). To characterize the thermal trimming, the MZI transmission spectrum was measured repeatedly throughout the trimming process; the phase shift and average effective index change (Δn_{eff}) were extracted from shifts in the fringes of the MZI spectrum. For each MZI spectrum measurement, the trimming process was paused, allowing the chip to cool to ambient temperature, and the input wavelength was scanned from 540-580nm while the

output optical power was measured. After 1 minute at 40mW of power dissipation in the heaters, phase trimming of about 500° was observed, corresponding to Δn_{eff} of about -0.0015. After 10 minutes, Δn_{eff} was about -0.0036. Over 97 days, the effective index was stable to within $<10^{-4}$ (measurement error limited). At a low heater power of 2mW (comparable to P_n), no significant thermal trimming was observed, indicating that the suspended heaters may be used as both TO phase shifters and trimming sections.

MEMS cantilevers with embedded waveguides: Electro-thermally actuated MEMS cantilevers were also realized with the suspended regions in Fig. 1(b) [16,17]. Each cantilever consisted of SiO₂ with an embedded heater, Al (M2) metal layer, and a SiN waveguide terminated with a grating coupler emitter. Heating from the TiN caused deflection of the cantilever due to the thermal expansion coefficient difference between SiO₂ and Al, Fig. 1(b,d). The MEMS cantilevers were used for beam steering, Fig. 2(b); the optical beam emitted by the SiN grating coupler was deflected by up to 30° with 30mW of power dissipation (measured by far-field imaging). The abrupt change in the slope of $\Delta\theta$ vs. heater power in Fig. 2(b) is due to the cantilever contacting the undercut Si substrate at large $\Delta\theta$; deeper undercut etching may be used to avoid this and enable larger deflections. The 300, 500, and 1000 μm long cantilevers had resonance frequencies of 77.4, 24.8, and 5.7kHz, respectively. We have also demonstrated cascaded cantilever devices for two-dimensional beam steering, and an angular steering range of about $24^\circ \times 12^\circ$ was achieved. More details are in [17].

Active PIC: Figure 2(c) demonstrates the integration of multiple features in a simple PIC consisting of a thermally-tuned add-drop microring with a directional coupler power tap and monitor PD on the thru port. As the heater power was swept, thru port optical transmission and PD photocurrent measurements were consistent [14].

In conclusion, we have demonstrated a foundry-fabricated, visible-light integrated photonics platform with advanced functionalities including monolithically integrated broadband photodetectors, efficient thermo-optic phase shifters, *in situ* thermal trimming, and electro-thermally actuated MEMS cantilever devices for optical beam steering. We are currently working on heterogeneous integration of lasers and high bandwidth electro-optic modulators onto the platform. This work opens an avenue toward the realization of complex PICs for visible and near infrared light applications.

References

- [1] A. Z. Subramanian et al., "Low-loss singlemode PECVD silicon nitride photonic wire waveguides for 532–900 nm wavelength window fabricated within a CMOS pilot line," *IEEE Photonics J.* 5, 2202809 (2013).
- [2] W. D. Sacher et al., "Visible-light silicon nitride waveguide devices and implantable neurophotonics probes on thinned 200 mm silicon wafers," *Opt. Express* 27, 37400–37418 (2019).
- [3] C. Sorace-Agaskar et al., "Versatile silicon nitride and alumina integrated photonic platforms for the ultraviolet to short-wave infrared," *IEEE J. Sel. Top. Quantum Electron.* 25, 1–15 (2019).
- [4] K. K. Mehta et al., "Integrated optical multi-ion quantum logic," *Nature* 586, 533–537 (2020).
- [5] W. D. Sacher et al., "Implantable photonic neural probes for light-sheet fluorescence brain imaging," *Neurophotonics* 8, 1–26 (2021).
- [6] D. Kohler et al., "Biophotonic sensors with integrated Si₃N₄-organic hybrid (SiNOH) lasers for point-of-care diagnostics," *Light Sci. Appl.* 10, 64 (2021).
- [7] M. Raval et al., "Integrated visible light phased array system for autostereoscopic image projection," *Opt. Lett.* 43, 3678–3681 (2018).
- [8] M. Notaros et al., "Integrated visible-light liquid-crystal phase modulator," in *Frontiers in Optics 2018*, p. FW6B–5.
- [9] G. Liang et al., "Robust, efficient, micrometre-scale phase modulators at visible wavelengths," *Nat. Photon.* 15, 908–913 (2021).
- [10] M. Dong et al., "Piezo-optomechanical cantilever modulators for VLSI visible photonics," *APL Photonics* 7, 051304 (2022).
- [11] S. Yanikgonul et al., "Integrated avalanche photodetectors for visible light," *Nat. Commun.* 12, 1834 (2021).
- [12] C. A. A. Franken et al., "Hybrid-integrated diode laser in the visible spectral range," *Opt. Lett.* 46, 4904–4907 (2021).
- [13] Y. Lin et al., "Low-loss broadband bi-layer edge couplers for visible light," *Opt. Express* 29, 34565–34576 (2021).
- [14] Y. Lin et al., "Monolithically integrated, broadband, high-efficiency silicon nitride-on-silicon waveguide photodetectors in a visible-light integrated photonics platform," *Nat. Commun.* 13, 6362 (2022).
- [15] Z. Yong et al., "Power-efficient silicon nitride thermo-optic phase shifters for visible light," *Opt. Express* 30, 7225–7237 (2022).
- [16] S. S. Azadeh et al., "1D beam steering by a waveguide-integrated MEMS cantilever in the visible spectrum," in *CLEO 2022*, p. AM2C.4.
- [17] S. S. Azadeh et al., "Microcantilever-integrated photonic circuits for broadband laser beam scanning," *arXiv: 2207.12374* (2022).
- [18] Z. Lu et al., "Michelson interferometer thermo-optic switch on SOI with a 50- μW power consumption," *IEEE Photonics Technol. Lett.* 27, 2319–2322 (2015).